

PAPER • OPEN ACCESS

Enhancement of Radiative Cooling Effect by Bioinspired Hollow-core Triangular Structures

To cite this article: Ke Li *et al* 2022 *J. Phys.: Conf. Ser.* **2185** 012007

View the [article online](#) for updates and enhancements.

You may also like

- [High-resolution simulations of the thermophysiological effects of human exposure to 100 MHz RF energy](#)
David A Nelson, Allen R Curran, Hans A Nyberg et al.
- [Double-end low-loss coupling of anti-resonant hollow-core fibers with solid-core single-mode fibers by tapering technique](#)
Hao Li, Wei Huang, Zefeng Wang et al.
- [Simplified human thermoregulatory model for designing wearable thermoelectric devices](#)
Dimuthu Wijethunge, Donggyu Kim and Woochul Kim



The Electrochemical Society
Advancing solid state & electrochemical science & technology

242nd ECS Meeting

Oct 9 – 13, 2022 • Atlanta, GA, US

Abstract submission deadline: **April 8, 2022**

Connect. Engage. Champion. Empower. Accelerate.

MOVE SCIENCE FORWARD



Submit your abstract



Enhancement of Radiative Cooling Effect by Bioinspired Hollow-core Triangular Structures

Ke Li^{1#}, Tianshun Zhang^{2#}, Lei Pan³, Xinyuan Zhang², Xiudong Xu², Shuliang Dou⁴, Yao Li⁴, and Yaohui Zhan^{2,5*}

¹Suzhou City University, Suzhou 215104, China.

²School of Optoelectronic Science and Engineering & Key Lab of Advanced Optical Manufacturing Technologies of Jiangsu Province, Soochow University, Suzhou 215006, China.

³School of Chemistry and Chemical Engineering, Harbin Institute of Technology, Harbin 150001, China.

⁴Center for Composite Materials and Structure, Harbin Institute of Technology, Harbin 150001, China.

⁵Light Industry Institute of Electrochemical Power Sources, Zhangjiagang 215600, China.

The authors contribute equally.

*Email: yhzhan@suda.edu.cn

Abstract. Inspired by the curiousness that what happens if the silver ant's hair is designed to be hollow-core rather than solid-core while maintaining its triangular shape, the thermoregulatory response of both the solid- and hollow-core schemes are investigated comprehensively in a photothermal viewpoint. Optical responses, power balances, and field distributions collectively show that the hollow-core system has many advantages over the solid-core system in terms of selective reflection, omnidirectional absorption capability, and overall cooling performance. The investigation sheds more light on the physics in the hollow-core structures and suggests an alternative biomimetic scheme for thermal management.

1. Introduction

Radiative cooling has attracted more and more attention in recent years [1-4], especially since the first daytime radiative cooler was demonstrated under direct sunlight [5]. As a dynamic thermal radiation process, radiative cooling can take the heat from the terrestrial object (hot end) to deep space (cold end) through the atmospheric window spontaneously, which is exactly why we feel cooler at night [6]. However, during the daytime, radiative cooling is quite challenging, which is mainly due to incoming solar radiation typically overpowers outgoing radiation to space and produces a net gain of thermal energy [7]. Therefore, reflecting more solar radiation and simultaneously pumping out more thermal emissions are essential requirements for daytime cooling [8]. So far, although challenging, various radiative coolers have been developed theoretically or experimentally, which fall into two categories: sandwichlike inorganic films [5, 9-11] and hybrid polymer films [12-16]. The former is represented by the multilayer film of silicon oxide and hafnium dioxide proposed by Fan group [5]; the latter is represented by the glass-bead mixed plastic membranes proposed by Hsu et al. [15] and the hierarchical porous polymer coatings by Mandal et al. [16]. Each kind of radiative cooler has its advantages; the



inorganic one has excellent mechanical properties and can be seamlessly integrated with the sophisticated vacuum process; the polymer one is flexible, scalable, and possible to get rid of the metallic back-reflectors. All these radiative coolers can be regarded as dual-band selective emitters satisfying the spectral requirements at different frequencies [17].

Recently, a similar artificial strategy of radiative cooling mentioned above has also been found in nature. It is reported that the silver ants can survive under extreme temperature conditions mainly due to a dense array of triangular hairs [as shown in figures. 1(a) and (b)], which enhance not only the reflectivity but also the emissivity of ants so as to keep their body cool even under direct solar irradiation [18]. The unique thermoregulatory solution of silver ants is coincident well with the requirement of radiative cooling discussed above. To explain the underlying physics, the hair of silver ants was modeled with a solid-core triangular cross-section, which agrees well with the measured results [18]. Most recently, the solid-core shape is further demonstrated experimentally by Q. Willot et al. [19]. However, as we all know, the hairs of many animals, e.g., polar bears, deer, and antelope, are hollow-core [20]. Therefore, a question is naturally aroused that what happens if the ant's hair is designed artificially to be hollow-core instead of solid-core.

To answer the question, in this work, a series of rigorous calculations and thorough comparisons are carried out for the two schemes in a photothermal viewpoint. The results demonstrate that the hollow-core systems have many advantages over their solid-core counterparts (e.g., higher solar reflection, stronger mid-infrared emission per volume) but also have some disadvantages, such as a lower total emissivity due to reduced material usage. The physics is uncovered by the full-wave optical simulations, and the final evaluation is attained by calculating the relative cooling powers. The further investigation shows that, although the hollow-core configuration is not dominant in terms of the overall emissivity, its solar reflectivity and emissivity per unit volume are much higher due to the rich cavity modes and the excellent spectral selectivity, and finally a relative cooling power of 45.76 W/m² of the hollow-core to the solid-core configuration is obtained, which suggests the hollow-core scheme can also be considered as a kind of potential biometric coatings for enhancing radiative cooling.

2. Model and Methods

The models are schematically shown in figure 1(c-d), where the ants' hairs with solid-core or hollow-core cross-sections are covered over the ants' head (mainly made from cuticle). Without loss of generality, the modeling parameters of solid-core triangular hairs are kept consistent with the reference [18]: the hairs are closely packed in a pitch of 2 μm , leaving an air-gap of 0.6 μm above the head surface; the height of the solid-core triangular cross-section is 2 μm . As for the hollow-core model, all the parameters are the same as the solid-core counterparts except the shell-thickness that is varied for optimization. The corrugation on the hair surface is not considered because it is trivial to physics (e.g., with little influence on the optical response) and complicated to reproduce in artificial coatings. Both TE (i.e., E-field is perpendicular to the plane of the paper) and TM (i.e., H-field is perpendicular to the plane of the paper) incidences are taken into consideration to reflect the random polarization feature of solar irradiation. The full-wave finite element method is employed by using Comsol Multiphysics [21].

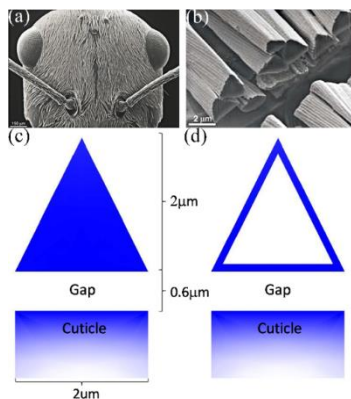


Figure 1. (a) SEM image of the head of Saharan silver ants covered with hairs. (b) Enlarged cross-sectional view of the hairs. (a) and (b) are reproduced with permission from [8], Copyright 2015, AAAS. (c) and (d) are the sketches of the models for ant hairs with solid-core and hollow-core cross-sections, respectively.

The reflected power of solar irradiance is calculated by weighting the standard AM1.5 spectrum as in Eq. 1,

$$P_{ref} = \int_0^{\infty} d\lambda R(\lambda) I_{AM1.5}(\lambda) \quad (1)$$

where R is the reflectance and IAM1.5 the standard AM1.5 spectrum. To evaluate the overall cooling capability, the net cooling power density (Pcool) is obtained from Eq. 2 as follows [5].

$$P_{cool}(T) = P_{rad}(T) - P_{atm}(T_{amb}) - P_{sun}(\theta_{sun}) - P_{cond+conv}(T, T_{amb}) \quad (2)$$

where $P_{rad}(T) = 2\pi \int_0^{\pi/2} d\theta \sin \theta \cos \theta \int_0^{\infty} d\lambda I_{BB}(T, \lambda) \varepsilon(\lambda, \theta)$ indicates the power density radiated out by the hair system, I_{BB} the spectral radiance of a blackbody, ε the spectral emissivity at incident θ ; T the temperature in the system; T_{amb} the ambient temperature; P_{atm} and P_{sun} stand for the power densities absorbed by the system due to atmospheric thermal radiation and solar irradiance, respectively; $P_{cond+conv}$ the density of power loss due to thermal conduction and convection. The formulas of P_{atm} , P_{sun} , and $P_{cond+conv}$ are listed briefly for completeness.

$P_{atm} = 2\pi \int_0^{\infty} d\theta \sin \theta \cos \theta \int_0^{\infty} d\lambda I_{BB}(T_{amb}, \lambda) \varepsilon(\lambda, \theta) \varepsilon_{atm}(\lambda, \theta)$, where ε_{atm} the spectral emissivity by the atmosphere. $P_{sun} = \int_0^{\infty} d\lambda \varepsilon(\lambda, \theta_{sun}) I_{AM1.5}(\lambda)$ where $\theta_{sun} = 0^\circ$ represents a direct solar illumination., $P_{cond+conv} = h_c(T_{amb} - T) = 103.5 \text{ W/m}^2$, where $h_c = 6.9 \text{ W} \cdot \text{m}^{-2} \cdot \text{K}^{-1}$, $T_{amb} = 315 \text{ K}$, and $T = 300 \text{ K}$ in the simulation. The structure's emissivity can be replaced by its absorptivity based on Kirchhoff's radiation law.

3. Results and Discussion

Firstly, the experimental refractive index of the silver ants' hair (i.e., $n \approx 1.56$) is considered according to ref. [18]. Figure 2 displays the reflection characteristics of the solid-core (gray) and hollow-core (red) systems in the wavelength range of $0.3 \mu\text{m}$ to $14 \mu\text{m}$. The non-polarized case is considered here by averaging the TE- and TM-polarized cases numerically. The wavelength axis is in the logarithmic scale to show the solar spectrum range clearer. As shown in figure 2 (a), the reflection spectra can be roughly divided into three regions: I) $0.3 \mu\text{m} - 1 \mu\text{m}$, where the reflectivity of the hollow-core configuration is much greater than the solid-core counterparts; II) $1 \mu\text{m} - 8 \mu\text{m}$, where the reflectivity of the solid-core configuration surpasses the hollow one; III) $8 \mu\text{m} - 14 \mu\text{m}$, where the reflectivities of the hollow-core and solid-core configurations are both kept lower than 3%. According to the requirement of radiative cooling, it is expected to reflect more solar light ranging from $0.3 \mu\text{m}$ to $2.5 \mu\text{m}$. Weighted by the standard AM1.5 spectrum, the reflected solar power is calculated based on Eq.1 for both configurations. As shown in figure 2(b), the reflected solar power of the hollow-core configuration (with a shell thickness of $0.1 \mu\text{m}$) is 166 W/m^2 , which is ~ 1.5 times that of the solid-core one (112 W/m^2), manifesting a noticeable improvement with the presence of hollow-core. The angular dependent reflected solar power is further calculated to ascertain the advantage of hollow-core systems beyond the normal incidence. As shown in figures 2(c) and (d), the reflected solar power of the hollow-core system is greater than the solid-core counterpart at most incident angles ($\theta < 20^\circ$ and $\theta > 45^\circ$), except in the range from 20° to 45° . The hollow-core system's enhancement ratio to the solid-core system is even higher than 1.5 at large incident angles (e.g., $\theta = 60^\circ \sim 80^\circ$).

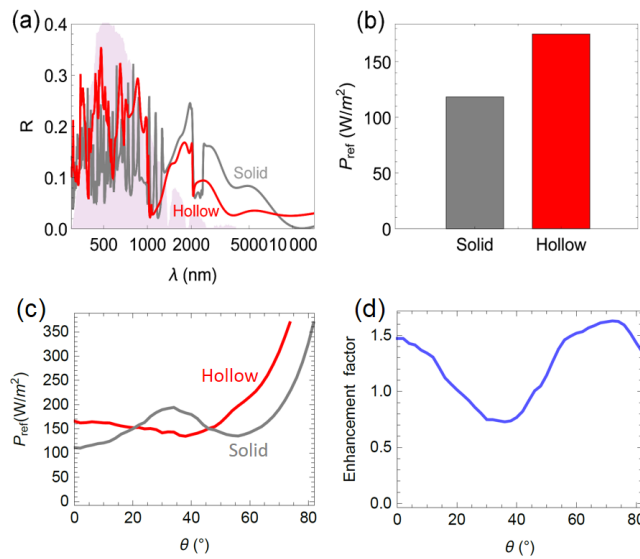


Figure 2. (a) Reflection characteristics of the solid-core (gray) and hollow-core (red) systems under direct sunlight; the pink shadow indicates the standard AM1.5 solar spectrum; the wavelength is in the logarithmic scale to show the solar spectrum clearer. (b) Reflected power densities of the solid-core (gray) and hollow-core (red) configurations. (c) Angular dependence of the reflected power density for hollow- and solid-core systems. (d) Enhancement ratio of the hollow-core to the solid-core system.

To explore the underlying physics behind the advantage of the hollow-core configurations in reflection, the light path and field distribution are investigated for both the individual and densely arrayed hair systems. For an intuition analysis, the typical light pathways are given in figure 3(a) for an individual hair, which shows that the light in the hollow-core system has more channels to be reflected than that in the solid-core system due to a doubled number of interfaces. As shown in figure 3(a), for the hollow-core triangular cross-section, there are two optical interfaces on each of three sides, where twice reflections occur when the light enters into (blue arrows) or escapes off (red arrows) the hair. From this perspective of geometric optics, the reflection would be improved and the transmission would be decreased accordingly. The prediction is verified by the full-wave calculations. As shown in figure 3(b), at an exemplified wavelength of 550 nm, the light intensity above (below) the hollow-core hair is much stronger (weaker) than that above (below) the solid-core one, indicating a much greater (smaller) reflection (transmission). The case of closely arrayed configurations is further considered in figure 3(c) at typical wavelengths of 480 nm, 648 nm, and 856 nm. As shown in figure 3(c), in the case of TE polarization, the cavity resonances that hold light back are very clearly observed in both systems; however, the resonance intensities are much stronger in the hollow-core system, resulting in a higher reflection. In the case of TM polarization, the focusing effect of triangular prisms makes light penetrate through the solid-core system more easily, leading to the high transmission and accordingly low reflection in the solid-core system. As discussed above, the physics underlying the hollow-core hair is ascribed to the optical cavity effect rather than the total internal reflection in the solid-core hairs under the oblique incidences.

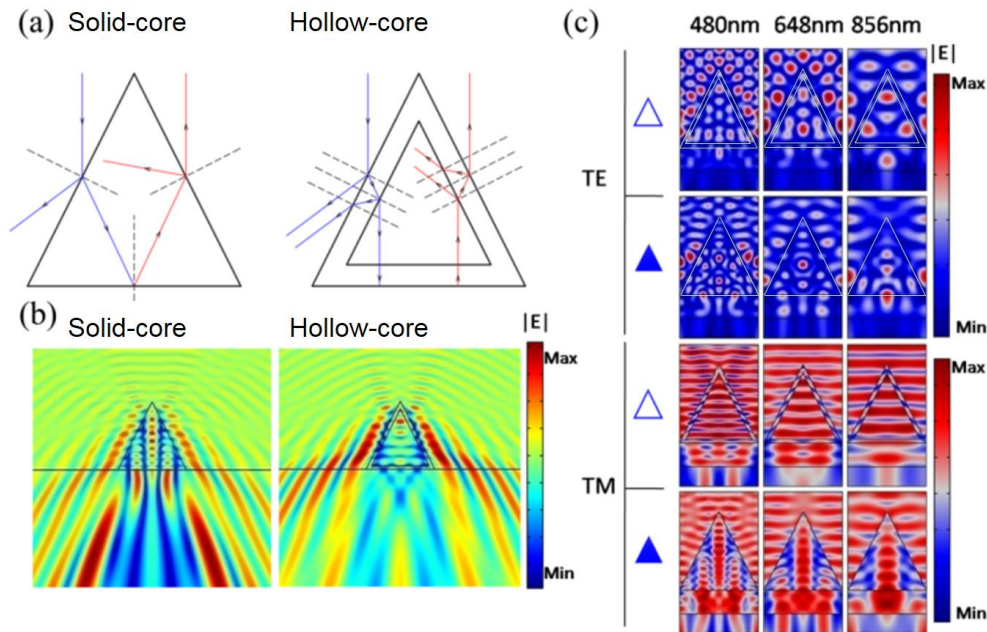


Figure 3. (a) Optical path diagrams of light that enters into (blue arrow) and escapes off (red arrow) an individual ant hair, from the viewpoint of geometrical optics. (b) Normalized electric fields in the individual-hair system with TE-polarized normal illumination at 550 nm. (c) Field distributions in the densely arrayed hair system at some exemplified wavelengths.

To take account of the case involving material absorption and dispersion, in the following, the material of hair structure is replaced by silica, which is widely utilized in the radiative cooling application due to its high extinction coefficient in the mid-infrared region [22]. The influence of the shell-thickness on the full optical responses (i.e., the reflectance, transmittance, and absorbance) and the corresponding power energies as a function of shell-thickness are displayed in figures 4(a-d), respectively. The spectra are shifted uniformly to make the spectral evolution clearer. As the shell is thin (e.g., 50 nm), the reflectivity is relatively weak [as shown in figure 4(a)] since the shell is too thin to form the cavity walls to eventually bounce light backward; in the meanwhile, the absorptivity (which quantitatively equals emissivity) is also small due to such a tiny volume [as shown in figure 4(c)]; as a result, most light is transmitted through the hairs [as shown in figure 4(b)]. As the shell increases to a moderate thickness (e.g., 0.1 μm), rich cavity resonances occur, and most of the reflection peaks are located in the visible range where solar irradiation accumulates. As the shell thickness is further increased, the reflection peaks redshift, resulting in reduced effective reflection by weighting the solar intensity. As for the emissivity in the mid-infrared, it can be seen from figure 4(c) that, it is gradually enhanced as the shell thickness increases and reaches the maximum with a solid-core substitutional structure, indicating that all the hollow-core configurations have a relatively lower total emissivity as compared to the solid-core counterparts mainly due to reduced material consumption. The detailed data for both the absolute and relative power densities can be referred to in table. 1.

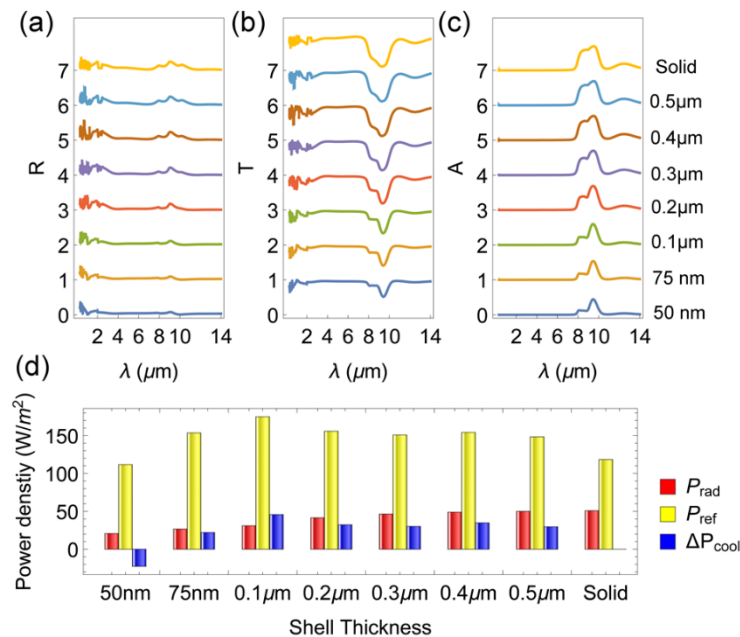


Figure 4. The reflectance (a), transmittance (b), and absorption (c) spectra for the hollow-core structures with different shell thicknesses. (d) The radiated (P_{rad}) and reflected (P_{ref}) power densities of the hollow-core systems and the difference of cooling power density (ΔP_{cool}) between the hollow-core and solid-core systems.

For quantitatively evaluated the broadband optical performances, the power densities as a function of shell thickness are calculated and displayed in figure 4 (d). It can be seen from figure 4 (d) that, as the shell thickness increases the reflected power by the hollow-core structure climbs up first and then descends, with a maximum of 174.87 W/m² at a thickness of 0.1 μm . As for the solid-core system, the reflected power is no more than 68% of the optimized hollow-core system. On the other side, the radiated power augments monotonously as the shell thickness increasing, showing a positive correlation with material consumption. To evaluate the overall cooling enhancement of the hollow-core structures with respect to the solid-core counterparts, a power difference ΔP_{cool} is defined as, $\Delta P_{\text{cool}} = P_{\text{cool}}(\text{hollow}) - P_{\text{cool}}(\text{solid})$ where the $P_{\text{cool}}(\text{hollow})$ and $P_{\text{cool}}(\text{solid})$ are the absolute cooling powers for the solid-core and hollow-core system, respectively. As shown in figure 4(d), as the shell is as thin as 50 nm, the ΔP_{cool} presents a negative value (- 22.65 W/m²), indicating that the potential cooling power of the hollow system is less than the solid-core one. As the shell becomes thicker, the cooling enhancement of the hollow system surpasses the solid-core system gradually and achieves a prominent ΔP_{cool} value of 45.76 W/m² at a shell thickness of 0.1 μm . As the shell changes even thicker (e.g., > 0.1 μm), the advantage of the hollow-core system is slightly weakened, but is still good enough compared to the solid-core counterpart.

Table 1. Power densities as a function of shell thickness.

Thickness (μm)	P_{rad} (W/m ²)	P_{ref} (W/m ²)	P_{atm} (W/m ²)	ΔP_{cool} (W/m ²)
0.05	20.76	111.68	11.83	-22.65
0.075	26.60	153.55	14.75	22.14
0.1	31.03	174.87	16.89	45.76
0.2	41.52	155.80	21.73	32.32
0.3	46.48	150.86	23.94	30.13
0.4	48.92	154.23	25.02	34.86
0.5	50.04	148.38	25.52	29.63
Solid-core	50.86	118.37	25.96	0

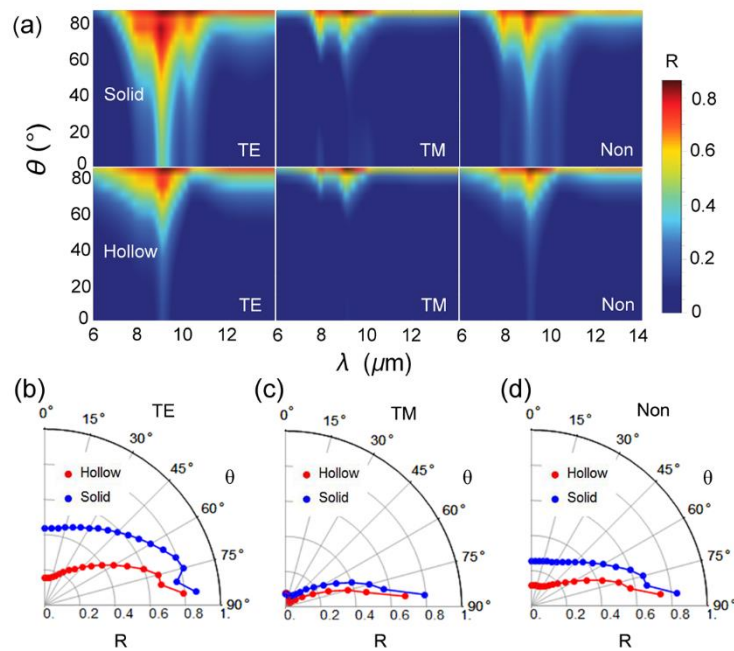


Figure 5. (a) The contour maps of reflection spectra versus the incident angle in the atmospheric window; The top and bottom rows correspond to the solid-core and hollow-core systems, respectively; The first, second, and third columns correspond to the TE, TM, and non-polarizations, respectively. The azimuthal reflection for the hollow-core (red) and solid-core (blue) arrayed structures at a wavelength of $9.05 \mu\text{m}$ under TE- (b), TM- (c), and non-polarization (d) incidences.

To get a full appreciation, the azimuthal reflectances for both the solid-core and the hollow-core arrayed configurations are extracted further, which indicates that an excellent feature of selective reflection can also be found in the hollow-core system. Since the emissivity quantitatively equals absorptivity, i.e., $\varepsilon = A = 1 - R - T$, the spectral reflection in the mid-infrared is expected to be as low as possible for a better emissivity enhancement. As shown in figure 5(a), the reflection of the hollow-core system is indeed lower than the solid-core one under either TE, TM, and non-polarization conditions. For showing clearer, the reflectance as a function of azimuthal angle is given in figures. 5(b-d) for TE, TM and non-polarization cases. The examined wavelength is fixed at $9.05 \mu\text{m}$, corresponding to a shared peak position in the reflection spectra [as shown in figure 4(a)] for both systems. As shown in figures 5(b-d), at any incident angles, the reflection of the hollow-core system is more or less lower than that of the solid-core system. Such an omnidirectional low reflection in the atmospheric window is exactly desirable as expected, which would facilitate the emission out of the system.

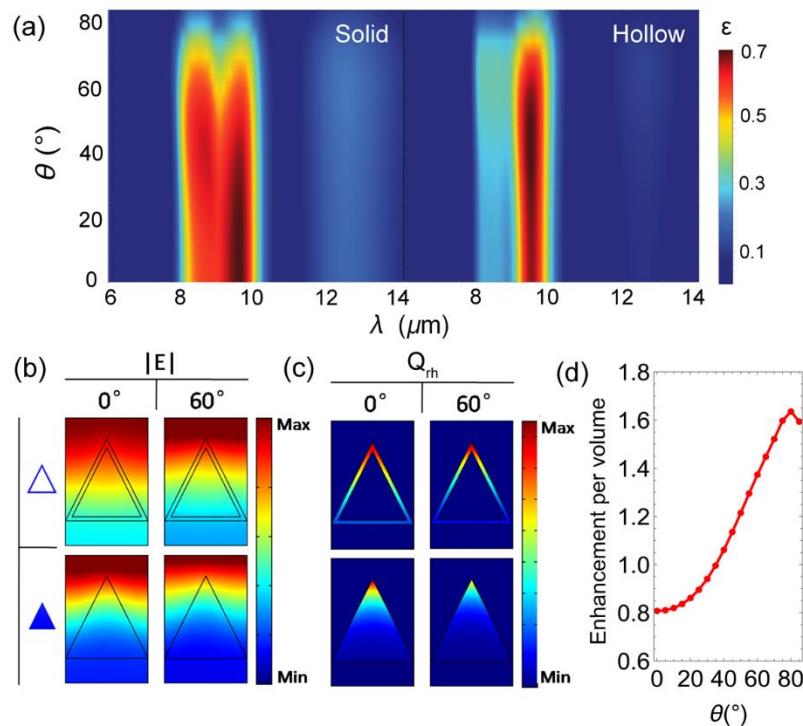


Figure 6. (a) The emission spectra of the solid-core (left) and hollow-core (right) arrayed structures as a function of incident angles under non-polarization illumination. The electric field (b) and absorption profiles (c) at typical incident angles. (d) The enhancement in absorption per volume as a function of incident angles.

Figure 6(a) displays the azimuthal emissivity for both the solid-core and the hollow-core arrayed configurations, which shows that the emissivity peak of the hollow-core system is much narrower than the solid-core counterpart on the whole. However, the maximal emissivity (e.g., at 9.05 μm) of the hollow-core system is almost the same as that of the solid-core, which is also preserved to a much larger angle compared to the solid-core. To reveal the microscopic information, figures 6(b-d) give the field distribution and absorption profile of both systems at a typical wavelength of 9.05 μm and representative incident angles of 0° and 60° . As shown in figure 6(b), in either case of 0° or 60° , the wavefront is straight (curved) in the hollow-core (solid-core) system, indicating the light field is hardly (greatly) distorted in the landscape orientation, which can be explained by the change of effective permittivity in the corresponding orientation according to Maxwell-Garnett approximation [23]. Benefited from the lower reflection, that light can penetrate deeper into the hollow-core structure. As a result, as shown in figure 6(c), the dissipation of light energy (Q_{rh}) into the edges of the hollow-core structure is in fact much stronger than that into the corresponding part of the solid-core structure. Finally, to evaluate the emission capability objectively, the volume of the active material is considered; the enhancement factor is defined as the ratio of the emission per unit volume for the hollow-core system to that for the solid-core system. As shown in figure 6(d), at a small incident angle, the enhancement ratio is less than unity (e.g., ~ 0.8 at 0°), indicating the emission per unit volume of the hollow-core system is smaller than that of the solid-core system. As the incident angle enlarges, the enhancement ratio increases rapidly, which surpasses unity at 35° and then reaches the summit of 1.65 at 80° . The results show that even though the material consumption is reduced by more than two-thirds, the emission per unit volume of the hollow-core system can even surpass the solid-core system at most angles, demonstrating an excellent emission capability.

4. Conclusions

In summary, inspired by Saharan silver ants' hair structure, we investigated the radiative cooling enhancement of the solid-core and hollow-core triangular schemes detailedly in a photothermal viewpoint. Based on comprehensive calculations, results collectively suggest that the hollow-core system possesses many advantages: firstly, more solar power can be reflected, nearly equaling to 1.5 times that of the solid-core system, due to the rich cavity resonances that are mainly benefited from the doubled optical interfaces. Secondly, even with a dramatic reduction of material consumption, a superb emission capability is preserved especially at large azimuthal angles. Last but not least, an important feature of selective reflection is observed in the spectral response, which is perfect-matched to the requirement of radiative thermoregulation. The investigation suggests a possible bio-inspired scheme for enhancing passive cooling, thermoregulation, and other relevant applications.

Acknowledgments

This work was supported by National Natural Science Foundation of China (62175174), the Natural Science Foundation of Jiangsu Province (BK20181167, BK20180208), Opening Project of State Key Laboratory of High Performance Ceramics and Superfine Microstructure (SKL201912SIC), the Priority Academic Program Development (PAPD) of Jiangsu Higher Education Institutions, the Natural Science Foundation of the Jiangsu Higher Education Institutions of China (18KJD416001), and the Qing Lan Project of the Jiangsu Province.

References

- [1] Chen Z, Zhu L, Li W, and Fan S 2019 *Joule* **3**(1): 101–110
- [2] Zhao B, Hu M, Ao X, Chen N, and Pei G 2019 *Appl. Energ.* **236** 489–513
- [3] M. Zeyghami, D. Y. Goswami, and E. Stefanakos, 2018 *Sol. Energ. Mat. Sol. C* **178**, 115–128
- [4] H. Ma, K. Yao, S. Dou, M. Xiao, M. Dai, L. Wang, H. Zhao, J. Zhao, Y. Li, and Y. Zhan 2020 *Sol. Energ. Mat. Sol. C* **212**, 110584
- [5] A. P. Raman, M. A. Anoma, L. Zhu, E. Rephaeli, and S. Fan *Nature* 2014 **515**(7528), 540–544
- [6] Md. M. Hossain and M. Gu, 2016 *Adv. Sci.* **3**(7), 1500360
- [7] W. Li, Y. Shi, K. Chen, L. Zhu, and S. Fan, 2017 *ACS Photonics* **4**(4), 774–782
- [8] E. Rephaeli, A. Raman, and S. Fan, 2013 *Nano Lett.* **13**(4), 1457–1461
- [9] J. Kou, Z. Jurado, Z. Chen, S. Fan, and A. J. Minnich, 2017 *ACS Photonics* **4**(3), 626–630
- [10] M. Zeyghami, E. Stefanakos, and D. Y. Goswami, 2017 *Sol. Energ. Mat. Sol. C* **163**, 191–199
- [11] L. Zhu, A. P. Raman, and S. Fan, 2015 *PNAS* **112**(40), 12282–12287
- [12] P. Hsu, C. Liu, A. Song, Z. Zhang, Y. Peng, J. Xie, K. Liu, C. Wu, P. Catrysse, L. Cai, S. Zhai, A. Majumdar, S. Fan, and Y. Cui, 2017 *Sci. Adv.* **3**(11), e1700895
- [13] L. Cai, A. Song, P. Wu, P. Hsu, Y. Peng, J. Chen, C. Liu, P. Catrysse, Y. Liu, A. Yang, C. X. Zhou, C. Y. Zhou, S. Fan, and Y. Cui, 2017 *Nat. Commun.* **8**, 496
- [14] P. Hsu, A. Song, P. Catrysse, C. Liu, Y. Peng, J. Xie, S. Fan, and Y. Cui, 2016 *Science* **353**(6303), 1019–1023
- [15] Y. Zhai, Y. Ma, S. David, D. Zhao, R. Lou, G. Tan, R. Yang, and X. Yin, 2017 *Science* **355**(6329), 1062–1066
- [16] J. Mandal, Y. Fu, A. Overvig, M. Jia, K. Sun, N. Shi, H. Zhou, X. Xiao, N. Yu, and Y. Yang, 2018 *Science*, **362**(6412), 315–319
- [17] K. Yao, H. Ma, M. Huang, H. Zhao, J. Zhao, Y. Li, S. Dou, and Y. Zhan, 2019 *ACS Appl. Nano Mater.* **2**(9), 5512–5519
- [18] N. N. Shi, C. Tsai, F. Camino, G. D. Bernard, N. Yu, and R. Wehner, 2015 *Science* **349**(6245), 298–301
- [19] Q. Willot, P. Simonis, J. P. Vigneron, and S. Aron, 2016 *PLoS One*, **11**(4), e0152325
- [20] Y. Cui, H. Gong, Y. Wang, D. Li, and H. Bai, 2018 *Adv. Mater.* **30**(14), 1706807
- [21] Comsol Multiphysics, <http://www.comsol.com>. Accessed 6 Jun. 2019.

- [22] J. Kischkat, S. Peters, B. Gruska, M. Chashnikova, M. Klinkmuller, O. Fedosenko, S. Machulik, A. Aleksandrova, G. Monastyrskyi, Y. Flores, and W. Masselik, 2012 *Appl. optics*. **51**(28), 6789–6798
- [23] R. Ruppin, 2000 *Opt. Commun.* **182**(4), 273–279